International Journal of Nanomedicine

Dovepress
Taylor & Francis Group

Open Access Full Text Article

ORIGINAL RESEARCH

Synergistic Induction of Immunogenic Cell Death by Biomineralized Manganese and Bisphosphonates Enhances Anti-PD-L1 Therapy in Triple-Negative Breast Cancer

Xiuli Zhang[1,2,*], Nan Liu[1,2,*], Mingjing Wei[1,2], Chuanlai Yang[1,2], Yanhua Lin[1,2], Yarong Zeng[1,2], Yufang Li[1,2], Lizhi Zhou[1,2], Tingting Li[1,2], Qingbing Zheng[1,2], Hai Yu[1,2], Jun Zhang[1,2], Ying Gu[1,2], Ningshao Xia[1,2], Shaowei Li[1,2]

[1]State Key Laboratory of Vaccines for Infectious Diseases, XiangAn Biomedicine Laboratory, School of Public Health, Xiamen University, Xiamen, People's Republic of China; [2]National Institute of Diagnostics and Vaccine Development in Infectious Diseases, State Key Laboratory of Molecular Vaccinology and Molecular Diagnostics, Collaborative Innovation Center of Biologic Products, National Innovation Platform for Industry-Education Integration in Vaccine Research, The Research Unit of Frontier Technology of Structural Vaccinology of Chinese Academy of Medical Sciences, Xiamen, People's Republic of China

*These authors contributed equally to this work

Correspondence: Shaowei Li; Ying Gu, Email shaowei@xmu.edu.cn; guying@xmu.edu.cn

Background: Despite therapeutic benefits of anti-Programmed Death-Ligand 1 (PD-L1) therapy in triple-negative breast cancer (TNBC), low response rates and resistance limit its efficacy. Both manganese (Mn) and bisphosphonates (BPs) are known to induce immunogenic cell death (ICD). Strategies to synergistically enhance ICD induction and elucidate the underlying molecular mechanisms remain to be fully explored.

Methods: We analyzed the mode of apoptosis and immunogenicity of cancer cells post-treatment using Western blotting, flow cytometry, and confocal microscopy. RNA sequencing was employed to identify activated apoptotic pathways and elucidate the molecular mechanisms underlying ICD when Mn^{2+} and BPs act synergistically. In 4T1 tumor models, we evaluated the synergistic anti-tumor effect of Mn^{2+} and BPs with anti-PD-L1 antibodies.

Results: By leveraging the doping capacity of hydroxyapatite (HA) for Mn^{2+} and its high affinity for BPs, we developed MnHARis particles—a biocompatible slow-release system of biomineralized Mn^{2+} and risedronate (Ris). Compared to Mn2+ and Ris alone, MnHARis achieved a synergistic antitumor effect, manifesting as increased cytotoxicity (IC50 reduced by 17 times) and the emergence of more significant mitochondrial autophagic apoptosis (more pronounced nuclear fragmentation, increased ROS levels, significantly decreased ATP levels, depolarization of mitochondrial membrane potential, upregulation of autophagy markers (LC3B and Beclin), and obvious autophagosomes). MnHARis exerts its antitumor effects via the p38-MAPK pathway. Additionally, increased exposure of calreticulin and increased secretion of high mobility group box 1 indicated that MnHARis successfully induced ICD and promoted specific recognition and cross-presentation of damage-associated molecular patterns released by apoptotic tumor cells by activating dendritic cells and pattern recognition receptors, thereby altering TME of TNBC, increasing TILs, and sensitizing TNBC to anti-PD-L1 therapy.

Conclusion: MnHARis effectively synergizes Mn^{2+} and Ris to promote autophagic apoptosis and ICD, increasing TILs and sensitizing TNBC to anti-PD-L1 therapy, thus offering a new therapeutic strategy.

Keywords: breast cancer, tumor infiltrating lymphocyte, tumor microenvironment, immunotherapy, immune checkpoint inhibitor

Background

TNBC is an aggressive subtype of cancer with a "colder" TME, accounting for about 15% to 20% of all breast cancers and associated with poor survival outcomes.[1] This type of breast cancer is particularly aggressive, with a median overall

Received: 7 November 2024
Accepted: 18 March 2025
Published: 17 April 2025

survival (OS) of approximately 12 to 15 months once metastasis occurs.[2] Studies have shown that anti-PD-L1 antibody combined with standard improves overall survival in patients with metastatic triple-negative breast cancer compared to chemotherapy alone.[3–5] These findings may provide new treatment options for patients with this disease. The first large randomized controlled trial evaluating the clinical activity of immunotherapy in metastatic triple-negative breast cancer showed that patients receiving the combination therapy had an overall survival of 25 months, compared to 15.5 months for those receiving chemotherapy alone.[6] However, the benefits of combination immunotherapy appear to be limited to a subgroup of patients with at least 1% of tumor-infiltrating immune cells expressing PD-L1. In triple-negative breast cancer, which is highly heterogeneous and lacks distinct drug targets, multi-modal synergistic therapies involving tumor immunotherapy, which can increase TILs, may bring new hope to patients.[7] Specifically, the induction of ICD is crucial because ICD is accompanied by the release of damage-associated molecular patterns (DAMPs). After recognized by antigen-presenting cells, DAMPs can activate both innate and adaptive immune responses, thereby increasing the likelihood of inducing more TILs.[8] However, there are currently few available ICD-inducing drugs.

Bone tissue is the most common metastatic site for TNBC.[9] BPs are the main drugs for treating bone-related diseases. Many clinical studies have shown that BPs are potential anticancer drugs for breast cancer,[10,11] the effect of ICD induced by BPs monotherapy on improving the immunosuppressive TME of TNBC is limited. There are still some aspects that require further exploration to promote BPs as drug candidates for clinical breast cancer therapy: (1) The mechanism is not fully understood: BPs direct antitumor mechanism has not been fully elucidated. Further research is needed to understand how BPs directly affect processes such as proliferation, apoptosis, invasion, and metastasis of breast cancer cells. (2) Synergistic effects with other treatment modalities: Although studies have shown that BPs have synergistic effects with chemotherapy, endocrine therapy, etc, the synergistic effects of BPs with other emerging treatment modalities such as immunotherapy and targeted therapy also need to be further explored. The primary mechanism of BPs' direct anticancer activity is to induce apoptosis in tumor cells, inhibit tumor cell adhesion, invasion, and proliferation.[12] BPs can induce tumor cell apoptosis by generating ATP analogs or disrupting the mevalonate pathway. Blockade of the mevalonate pathway leads to a reduction in isoprenoids, which are essential for the prenylation of small GTPases (such as Ras) that are vital for many cancer cells.[13] BPs-induced mevalonate pathway disruption is associated with the release of cytochrome c from mitochondria into the cytoplasm, subsequently activating the caspase cascade reaction, leading to apoptosis in breast cancer cells.[14–16] In addition, BPs also exhibit indirect anticancer activity, such as inducing dose-dependent expansion of γδ T cells, driving tumor-associated macrophages towards M1-type differentiation, etc. BPs have synergistic effects with various anticancer drugs.[17] To date, dozens of clinical trials of BPs in oncology are underway, especially in breast cancer and prostate cancer. Combining BPs with various anticancer treatment strategies is a viable path to amplify the anticancer effects.

The metal-chelating properties of BPs make it possible to combine them with metal ions, thereby enhancing immunostimulatory effects and antitumor activity. Among these, Mn^{2+} is one of the noteworthy metal ions. Mn-based materials, have a simple composition and multiple functions to enhance tumor immunotherapy, including: 1) serving as a biocompatible nanocarrier to deliver immunotherapeutic agents, activating the host's immune system; 2) acting as an adjuvant to modulate the tumor immune microenvironment, promoting immune response; 3) activating the cGAS-STING pathway to initiate tumor immunotherapy; 4) MRI real-time monitoring of tumor immunotherapy effects.[18,19] However, direct coprecipitation of Mn^{2+} with BPs can produce good immunostimulation but also increases toxicity.[20] The main characteristic of HA is its ability to be doped with various ions, among which divalent metal cations, trivalent anionic groups, and monovalent anions can easily substitute into the crystal structure of stoichiometric apatite, thus altering its physical, chemical, and biological properties.[21] There are two main methods for synthesizing HA-doped materials: chemical adsorption and coprecipitation (mineralization).[22] Compared to chemical adsorption, mineralization can provide stronger interactions between the substituent and HA, thereby constructing a drug release system. Utilizing HA mineralization with Mn^{2+} and BP can enhance biocompatibility and may synergistically exert antitumor activity of Mn^{2+} and BPs.

Despite the potential efficacy of anti-PD-L1 therapy in TNBC patients, low response rates and an immunosuppressive TME remain major obstacles to its effectiveness. Mn^{2+} and BPs have the potential to induce ICD, thereby altering TME, increasing the number of tumor-infiltrating $CD8^+$ and $CD4^+$ T cells, and enhancing the efficacy of anti-PD-L1 therapy.

However, how to synergistically enhance ICD induction and the underlying molecular mechanisms and potential therapeutic strategies still need further elucidation. This study utilizes HA's high affinity for BPs and its doping characteristics for Mn^{2+} to construct a Mn^{2+} - BPs (Ris, [C7H10NNaO7P2]) biocompatible sustained-release system (MnHARis particles) through a coprecipitation mineralization method, attempting to further elucidate the collaborative induction of tumor cell death by the cGAS-STING pathway and the mevalonate pathway and the potential cytotoxic mechanisms. Using Western blot, flow cytometry (FCM), and confocal microscopy, we analyzed the apoptosis patterns and immunogenicity of cancer cells after treatment. RNA sequencing was used to analyze the potential apoptosis pathways and molecular mechanisms of ICD activated by the synergistic effect of Mn^{2+} and BPs. In the 4T1 tumor-bearing mouse model and human liver cancer xenograft model, the induction of tumor-infiltrating T cell immune after combined treatment with Mn and BPs and its combination effect with anti-PD-L1 antibody therapy were evaluated.

Materials and Methods

Materials

$CaCl_2$, $MnCl_2$, Na_2HPO_4, NaOH, ethanol, and urea were procured from Xilong Chemical Company. Ris was sourced from Hunan HuaTeng Pharmaceutical. Fetal bovine serum, penicillin/streptomycin antibiotic and prestained protein ladder were supplied by Thermo Fisher Scientific. Phosphate-buffered saline (PBS), MEM non-essential amino acids, RPMI 1640, and trypsin were acquired from Shanghai Basalmedia Technologies. All antibodies used in FCM and tumor immunohistochemistry were sourced from BioLegend. BCA kits, Cell Counting Kit-8, crystal violet, propidium iodide (PI), Annexin V-FITC/PI assay kit, and ATP assay kit were obtained from Beyotime. The terminal deoxynucleotidyl transferase dUTP nick end labeling (TUNEL) assay kit was purchased from Promega. AO/EB staining assay was sourced from Shanghai Mao-kang Co., LTD. CYTO-ID autophagy detection kit was obtained from Enzo Life Sciences. Calreticulin (CRT) ELISA kit and high-mobility group protein (HMGB1) ELISA kit were procured from Shanghai Jianglai Biotechnology Co., LTD and Wuhan Fine Biological Technology Co., LTD, respectively.

Cytotoxicity Test

All cell lines used in this study are from ATCC (4T1: CRL-2539, EMT6: CRL-2755, Hela: CRM-CCL-2, Caski: CRM-CCL-1550, SiHa: HTB-35, B16F10: CRL-6475, HepG2: HB-8065, CT26: CRL-2638), except the MC38 cells is from Wuhan Scion Biotechnology Co. LTD (SNL-505). The cervical cancer patient-derived organoids (PDO) were prepared as described in the literature.[23] The half-maximal inhibitory concentration (IC_{50}) was determined using the Cell Counting Kit-8 (CCK8). Cells (1×10^4) were seeded in 96-well plates and treated with various concentrations of $MnCl_2$, Ris, MnRis, and MnHARis for 48 hours. The concentration range for the drugs (Mn^{2+}, Ris, MnRis, MnHARis) used is 10–10^4 nM. After medium exchange, CCK8 reagent was added at a 1:10 ratio, and optical density was measured at 450 nm using a microplate reader. The IC_{50} values were calculated for subsequent dosing experiments.

Cell Apoptosis Analysis

In the following cell-related experiments, the Mn^{2+} concentration used is 150 μM, the Ris concentration used is 75 μM, and the MnHARis adjuvant is diluted 100-fold (Note: The concentration of Mn^{2+} and Ris contained in the 100-fold diluted MnHARis adjuvant is consistent with 50 μM Mn^{2+} and 75 μM Ris. Cell apoptosis was analyzed using confocal laser scanning microscopy (CLSM, Leica, TCS SP8 X) and FCM (BD, FortessaX-20). 4T1 cells were co-cultured with $MnCl_2$, Ris, MnRis, and MnHARis for 48 hours in 96-well plates, followed by AO/EB and 4′,6-diamidino-2-phenylindole (DAPI) staining according to the manufacturer's instructions. Briefly, cells were incubated with AO/EB or DAPI solution in the dark for 15 minutes, then washed thrice with PBS. Morphological observations were recorded using CLSM. For FCM, similar procedures were followed, except cells were cultured in 24-well plates.

Detection of Intracellular Reactive Oxygen Species (ROS) by CLSM

CLSM was used to detect intracellular ROS in 4T1 cells. Cells were seeded in 96-well culture plates at a density of 8×10^4/mL and cultured for 24 hours before treatment. Groups received PBS, $MnCl_2$, Ris, MnRis, and MnHARis, and were

cultured for another 24 hours. DCFH-DA was diluted to a final concentration of 10 μM, incubated for 20 minutes, and cells were washed thrice to remove unbound DCFH-DA before fluorescence photography.

Cyto-ID Staining

Cells were seeded on glass coverslips at a density of 1×10^5 cells/mL and stained with Cyto-ID Green for 30 minutes following treatment. Post-counterstaining with DAPI for 10 minutes, cells were observed under CLSM. For FCM-based autophagy detection, treated cells were harvested, stained with Cyto-ID, re-suspended in PBS, and analyzed via the FITC channel.

Western Blotting

Cells were lysed using a buffer containing protease inhibitors. Protein concentrations were determined using a BCA assay, and 30 μg of protein per sample was separated by SDS-PAGE. Transferred gels onto PVDF membranes were blocked with 5% bovine serum albumin for 4 hours. Primary antibodies were applied overnight at 4°C. Membranes were then incubated with appropriate secondary antibodies for 1 hour the next day, washed five times for 10 minutes each in Tris-buffered saline with tween, and target bands were visualized using the ECL detection system (Bio-Rad, USA). GAPDH served as an internal reference.

Cell Cycle Phases Analysis

4T1 cells treated with $MnCl_2$, Ris, MnRis, and MnHARis for 48 hours were analyzed using FCM after fixing with ice-cold 70% ethanol and staining with PI staining buffer (0.4 μg/mL PI in PBS). The cell cycle phase distribution was then determined by FCM.

Intracellular ATP Level Analysis

4T1 cells were cultured in 96-well plates at a density of 1×10^5 cells per well until approximately 80% confluence was reached. Different treatments were then applied and incubated for 48 hours. ATP levels were quantified using a commercial ATP assay kit employing the bioluminescence method.

Measurement of Mitochondrial Health by JC-1

Coverslips in 24-well plates with attached 4T1 cells received $MnCl_2$, Ris, MnRis, and MnHARis treatments and were incubated for 48 hours. Post-incubation, cells were washed with PBS, and 10 μM JC-1 was added to each well. After 20 minutes, cells were washed again with PBS, and fluorescent signals were detected using CLSM. FCM analysis of mitochondrial membrane potential was conducted similarly, sans coverslips.

In vitro Phagocytosis Assay

DC2.4 cells were labeled with Cell Tracker Red, and 4T1 tumor cells were labeled with Cell Tracker Green. 4T1 tumor cells (5×10^5) incubated with PBS, $MnCl_2$, Ris, MnRis and MnHARis for 48 h, and then were co-cultured with DC2.4 cells (1×10^5) for 8 h. After incubation, the percentage of phagocytosis was detected by FCM.

ICD Induced in vitro

4T1 cells treated with $MnCl_2$, Ris, MnRis, and MnHARis for 12 hours were analyzed for CRT and HMGB1 using the respective ELISA kits according to the manufacturer's instructions. For FCM analysis, cells were fixed, permeabilized, and blocked before incubation with FITC-labeled CRT or HMGB1 antibodies. For CLSM, cells were fixed with 100% methanol, permeabilized with Triton X-100, blocked, and then incubated with CRT-FITC antibody overnight at 4°C. Nuclear DNA was labeled with DAPI.

RNA Isolation and RNA-Seq Data Processing

5×10^6 4T1 cells treated with PBS, $MnCl_2$, Ris, MnRis, and MnHARis for 24 hours had total RNA extracted using the Total RNA Extractor Trizol kit. Sequencing libraries were prepared from 1 μg of RNA per sample using the VAHTS

mRNA-seq V2 Library Prep Kit for Illumina®, following the manufacturer's recommendations. Index codes were added to attribute sequences to each sample. Raw reads were cleaned by Trimmomatic, mapped to the reference genome by HISAT2, and analyzed for alignment quality by RSeQC and Qualimap. Differential gene expression was assessed using DESeq2, considering genes significantly differentially expressed if q-value ≤ 0.001 and |Fold Change| ≥ 2. For genes with zero expression in both samples, expression values were adjusted to 0.01 to enable plotting on a log scale.

Inhibitor Experiments

In the autophagy inhibition experiment, 4T1 cells were pre-treated with 5 mm 3-methyladenine (3-MA), 10 μM mdivi-1, 10 μM Wortmannin (Wor), 10 μM SB202190, 5 μM BAPTA-AM for 4 hours, and then co-incubated with MnHARIs for 48 hours. PBS treatment was used as a control. Cell viability was determined using the CCK8 assay as previously described, with the calculation formula: Cell viability = (OD450 of experimental well / OD450 of control well) * 100%.

In vivo Anti-Tumor Effect

The minimum sample size for animal experiments was calculated using the G*POWER software based on the number of experimental groups, the statistical analysis methods used, the significance level (0.05), and the statistical power (0.8). Mice were randomly assigned to groups using simple randomization. Outcome measures for in vivo anti-tumor experiments included tumor volume, survival time, weight change, and changes in tumor-infiltrating $CD4^+/CD8^+$ cells. For hypothesis testing studies, the outcome measures used to determine sample size were tumor volume and survival time. Female BALB/c mice (6–7 weeks old, healthy) were injected with 1×10^6 4T1 cells into the right dorsal side after hair removal. When the tumor volume reached 80 ~ 120 mm^3 (inclusion criteria), the mice were randomly divided into four groups (a total of 24 mice, 6 per group, n=6 per cage). Tumor intratumoral injections were administered every three days, with treatments consisting of 100 μg anti-PD1 antibody, 50 μL adjuvant (MnHARIs, diluted 1:1 v/v with saline), or a combination of the two (pre-mixed at 4°C for 24 hours), for a total of four treatments. The control group received 50 μL PBS, with MnHARIs, αPD-L1, and MnHARIs+αPD-L1 as the experimental groups. Tumor volume and survival time were recorded every three days. Mice were euthanized when the tumor volume reached 2000 mm^3. Tumors were then fixed in 4% paraformaldehyde, embedded in paraffin, and subjected to immunohistochemical analysis (IHC) for CD4 and CD8 expression. In the patient-derived xenograft (PDX) animal model of human hepatocellular carcinoma, 7-week-old NOD SCID mice (immunodeficient) were used. Inclusion criteria required the PDX tumor volume to reach 80–120 mm^3. A total of 6 mice were enrolled, randomly divided into two groups, with 3 mice per group, housed three per cage (n=3). The PBS group served as the control group, and the MnHARIs group served as the experimental group. PBS group (50 μL/dose) or MnHARIs group (50 μL/dose) was administered every 3 days (for a total of 4 doses, n=3). Mice treatment, weighing, and tumor measurement were carried out in a randomized sequence. Control and experimental group cages were placed on the same rack and kept under identical housing conditions. Grouping personnel and data analysts were aware of the group assignments, but personnel responsible for weighing, measuring, treating, and observing the mice were blinded to group assignments. All the mouse breeding and related experimental operations were carried out in SPF-grade animal rooms, with treatment, observation, and measurement procedures arranged by referencing previous PD-L1 related animal experiment articles. Tumor volumes were determined by caliper measurement according to the formula $W^2 \times L/2$ (L = length and W = the perpendicular width of the tumor, L > W).

Statistical Analysis

Data are expressed as means ± standard deviation (SD). Statistical analyses were performed using SPSS 24.0. Differences between two groups were assessed using Student's t-tests. Prior to comparing multiple groups, variance similarity tests (F-tests) were conducted. Homogeneous variances were compared using one-way ANOVA with LSD post-hoc tests; heterogeneous variances were compared using ANOVA with Dunnett's T3 post-hoc test. Survival curves were analyzed using the Kaplan–Meier method and Gehan–Breslow–Wilcoxon test. Statistical significance was defined as $^*p < 0.05$, $^{**}p < 0.01$, $^{***}p < 0.001$.

Results

MnHARis Induces a Stronger Apoptotic Effect in Tumor Cells

As shown in Supplementary Figure 1A, both MnRis and MnHARis are white suspensions, which settle after standing for 48 hours. In cell culture media and slightly acidic environments like tumors, MnRis and MnHARis exhibit negative zeta potential (Supplementary Figure 1B). Other physicochemical properties of MnRis and MnHARis particles can be referred to our previously published article.[20] In this study, we primarily focus on elucidating the antitumor effects and mechanisms of MnHARis. For 4T1 cells, the IC_{50} of MnHARis (50.23 nM) was markedly lower than that of $MnCl_2$ (848.45 nM), Ris (768.00 nM), and MnRis (254.30 nM) as indicated in Figure 1A and B. The cytotoxicity of MnHARis on the 9 tumor cell

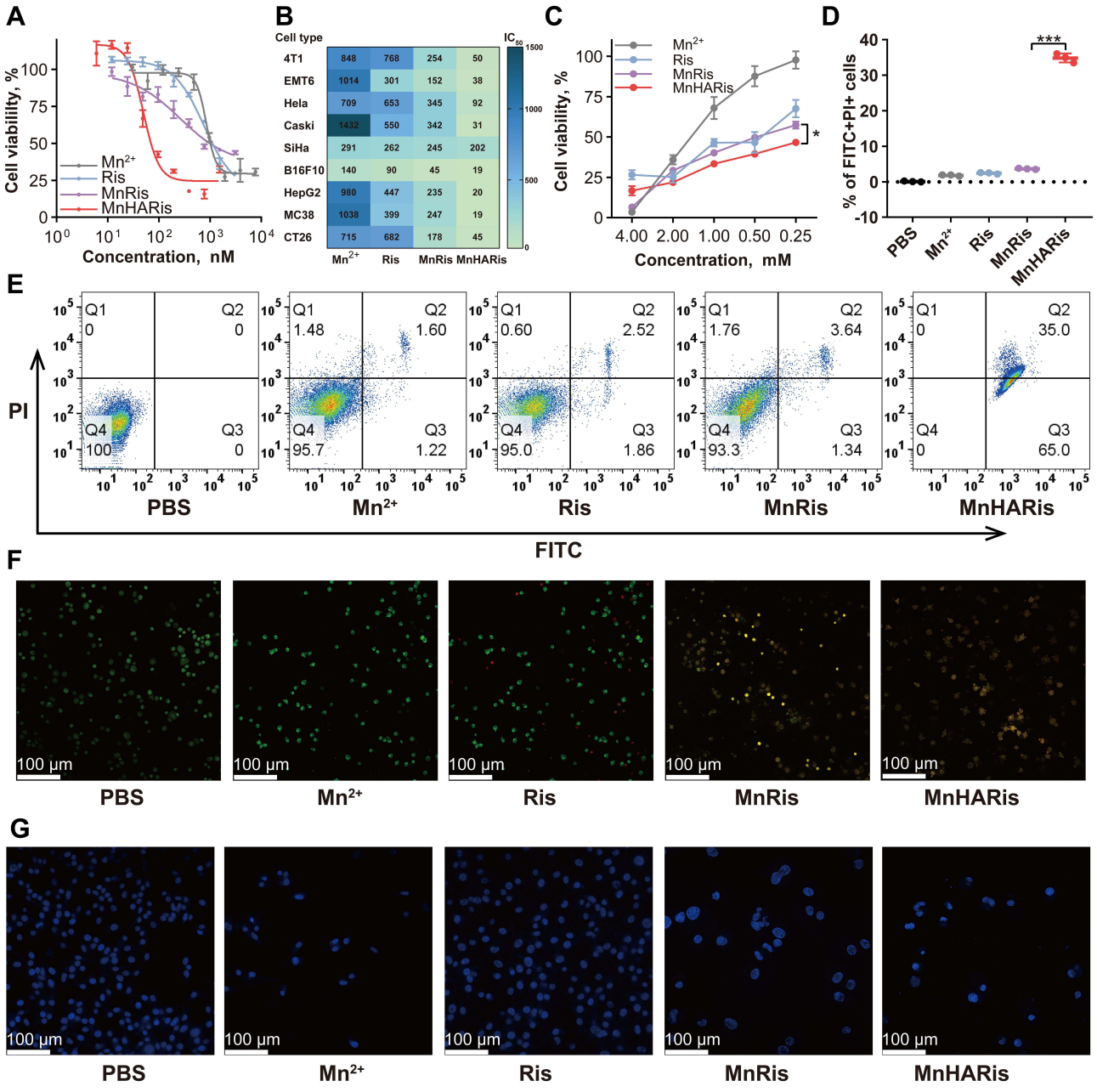

Figure 1 MnHARis induces apoptosis in tumor cells. (**A**) Cell viability of 4T1 tumor cells treated with Mn^{2+}, Ris, MnRis and MnHARis. (**B**) The cytotoxicity of Mn^{2+}, Ris, MnRis and MnHARis against 9 types of tumor cell lines. The numbers in the heatmap represent the IC_{50} (μM) values. (**C**) Cell viability of cervical cancer PDO after treated with Mn^{2+}, Ris, MnRis and MnHARis. Flow cytometric profiles (**D** and **E**) of 4T1 cells after incubation with PBS, $MnCl_2$, Ris, MnRis and MnHARis for 48 h. (**F**) AO/EB stain images and (**G**) DAPI stained fluorescent images of 4T1 cells treated with PBS, $MnCl_2$, Ris, MnRis and MnHARis for 48 h (scale bar=100 μm). Statistical significance was defined as *p < 0.05, **p < 0.01, ***p < 0.001.

lines tested was significantly higher than that of free Mn^{2+} and Ris, as well as MnRis formed by direct mineralization, indicating that MnHARis have better anti-tumor effect in vitro. In cervical cancer PDO, MnHARis retained its antitumor advantage (Figure 1C). FCM and CLSM were employed to analyze the apoptotic effects of MnHARis on 4T1 cells. Annexin V-FITC/PI double staining results show the early apoptotic cells (FITC+/PI-) and late apoptotic cells (FITC+/PI+) in the MnRis group were not significantly different from those in the Mn2+ and Ris groups (Figure 1D and E). However, the early apoptosis rate (64.5±0.8%) and late apoptosis rate (34.86%±0.3%) induced by MnHARis are 48.1 times and 10.6 times higher than those of MnRis, respectively. This indicates that MnHARis has a strong ability to induce tumor cell apoptosis. AO/EB staining for apoptosis detection also confirmed the induction of apoptosis. In the PBS and Mn2+ groups, there is a large amount of viable cells with green-stained nuclear chromatin, while a small number of necrotic cells with red-stained nuclear chromatin are observed in the Ris group (Figure 1F). In the MnRis group, a large amount of early apoptotic cells with condensed or bead-like green-stained nuclear chromatin and some orange-red late apoptotic cells can be seen. In contrast, fluorescence images of 4T1 cells treated with MnHARis show more orange-yellow late apoptotic cells and apoptotic bodies. Similarly, after DAPI staining, MnHARis-treated 4T1 cells exhibited more pronounced chromatin condensation and fragmentation, nuclear fragmentation, and irregular edges (Figure 1G). These findings clearly indicate that MnHARis is more effective in inducing apoptosis in 4T1 cells.

MnHARis Induces Mitophagy-Mediated Apoptosis

Mitochondrial dysfunction, mitophagy, and apoptosis have been suggested to be interrelated in various human carcinomas. Fluorescence microscopy was used to examine the effects of $MnCl_2$, Ris, MnRis and MnHARis on ROS in 4T1 cells. Results showed that the Ris group cells exhibited the least green fluorescence, and the intracellular ROS in the MnHARis group dramatically increased (Figure 2A). Overproduction of ROS can bring out changes in cell function. Next, we examined the changes of intracellular ATP. As shown in Figure 2B, compared with the control group, the intracellular ATP content decreased after different treatments with the MnHARis group showed the lowest ATP content. After that, we detected the changes in mitochondrial membrane potential. The results of FCM analysis found there was no significant difference in the effect of Mn^{2+} and Ris on mitochondrial membrane potential, but the damage was greater when MnRis was formed by the mineralization of both, with MnHARis having the most significant adverse effect on mitochondria (Figure 2C and D). Fluorescence microscopy and FCM were used to examine autophagosomes in 4T1 cells. Upon massive mitochondrial depolarization after MnHARis treatment, autophagosomes accumulated on 4T1 cells, suggesting MnHARis triggered mitophagy via ROS potentially (Figure 2E and F). Subsequently, the expressions of autophagy related proteins in total cellular proteins also confirmed the same results by Western blot, which showed that compared with the control group, treatment with MnHARis prominently increased LC3B-II and Beclin 1 levels in 4T1 cells (Figure 2G). Overall, the experimental results indicated that MnHARis was more likely to induce the production of ROS, decrease ATP level, cause mitochondrial dysfunction, induce mitophagy and eventually lead to apoptosis than the free Mn^{2+} and Ris and MnRis formed by direct mineralization of both.

MnHARis Induces ICD

In addition to inducing tumor cell apoptosis through mitophagy, MnHARis also has the advantage of promoting immune responses. Phagocytosis assays showed that 4T1 tumor cells treated with MnHARis were more readily engulfed by DC2.4 cells compared to those treated with Mn^{2+}, Ris, or MnRis, indicating potential immunogenic effects (Figure 3A and B). Calreticulin (CRT) exposure, a key marker of ICD,[24] was significantly increased in MnHARis-treated cells. As shown in Figure 3C, after treating 4T1 cells with MnHARis, the expression level of CRT was significantly increased, which was higher than that of the Mn^{2+} or Ris treatment group alone, and higher than that of the MnRis group. To further verify that CRT underwent membrane translocation after MnHARis treatment of 4T1 cells, we used FCM to measure the number of cells expressing CRT positively on the cell membrane surface. The results showed that the number of 4T1 cells expressing CRT on the surface was also the highest in the MnHARis group (Figure 3D and E). Next, CLSM was used to observe the CRT-specific green fluorescence intensity of cell membrane in different treatment groups. Consistent with the results of ELISA and FCM, the intensity of green fluorescence on the cell membrane was the strongest in the MnHARis group, highlighting effective CRT translocation to the cell membrane. This effect was significantly stronger

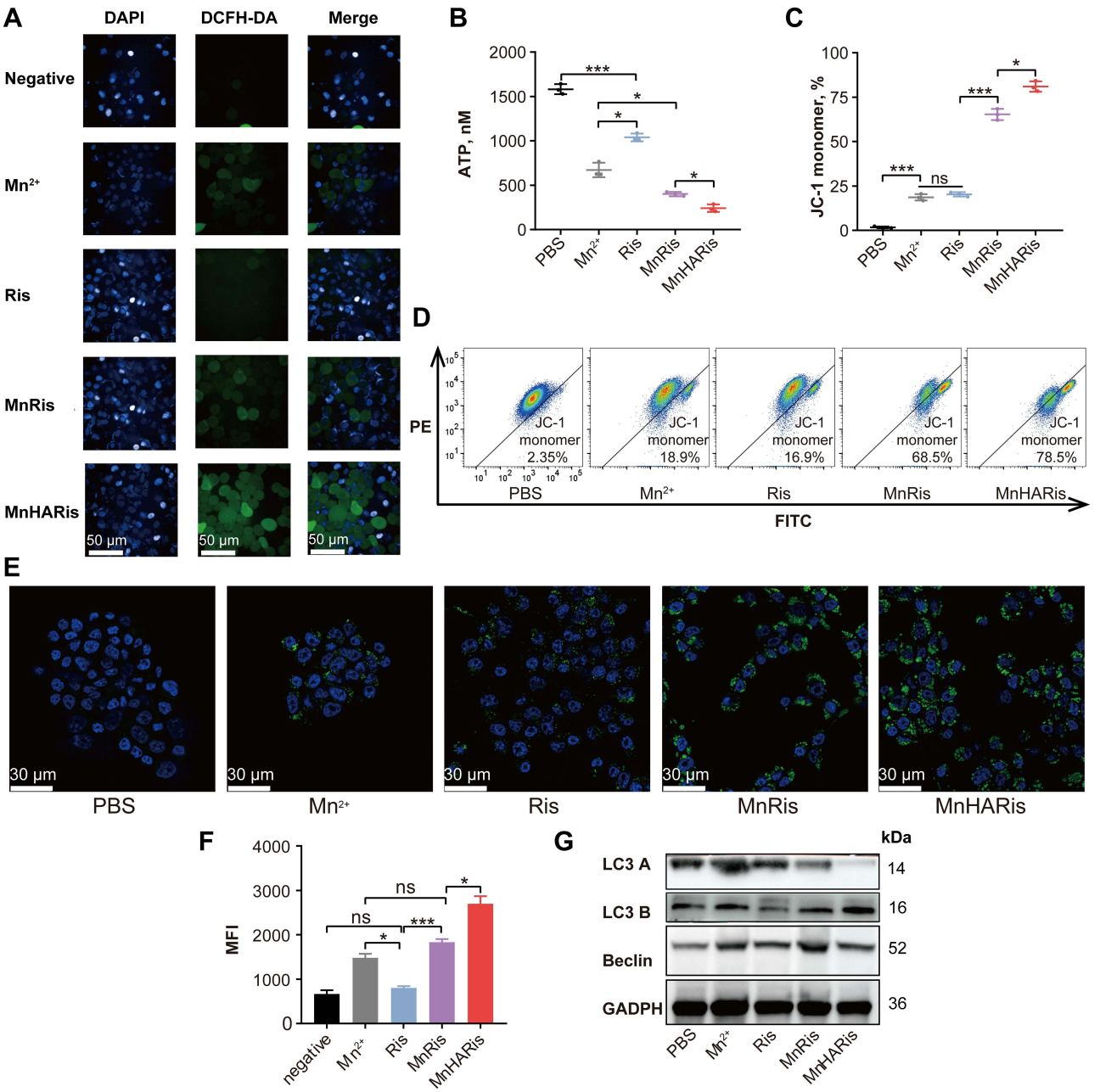

Figure 2 Evaluation of Cellular Stress and Autophagy Induction. (**A**) DCFH-DA staining detecting intracellular ROS with green fluorescence for ROS (DCFH-DA) and blue for nuclei (DAPI) (scale bar=50 μm). (**B**) Changes in ATP levels in 4T1 cells following various treatments. (**C**) Quantitative FCM analysis of mitochondrial membrane potential depolarization using JC-1 dye and the (**D**) representative pictures. (**E**) CLSM images of autophagosomes in treated cells visualized with Cyto-ID Green staining; nuclei stained blue with DAPI (scale bar: 30 μm). (**F**) Cyto-ID staining results analyzed using FCM. (**G**) Western blots displaying levels of autophagy-associated proteins with GAPDH as the loading control. Statistical significance was defined as *p < 0.05, **p < 0.01, ***p < 0.001.

than that of Mn^{2+} or Ris alone, and also stronger than that of MnRis. During the process of cell apoptosis, HMGB1 translocates from the nucleus to the cytoplasm, is released into the extracellular space through the plasma membrane, and interacts with receptors such as TLR4 to activate the antigen-presenting function of mature DCs.[25] In this study, we used ELISA and FCM to detect the content of HMGB1 and found that, compared with the control group cells treated with PBS, the content of HMGB1 in cells treated with different factors was significantly increased, and the MnHARis group had the highest amount of HMGB1 (Figure 3F–H). Thus, MnHARis effectively initiated both innate and adaptive immune responses through ICD, characterized by CRT exposure and HMGB1 secretion, leading to enhanced uptake of tumor cell debris by DCs.

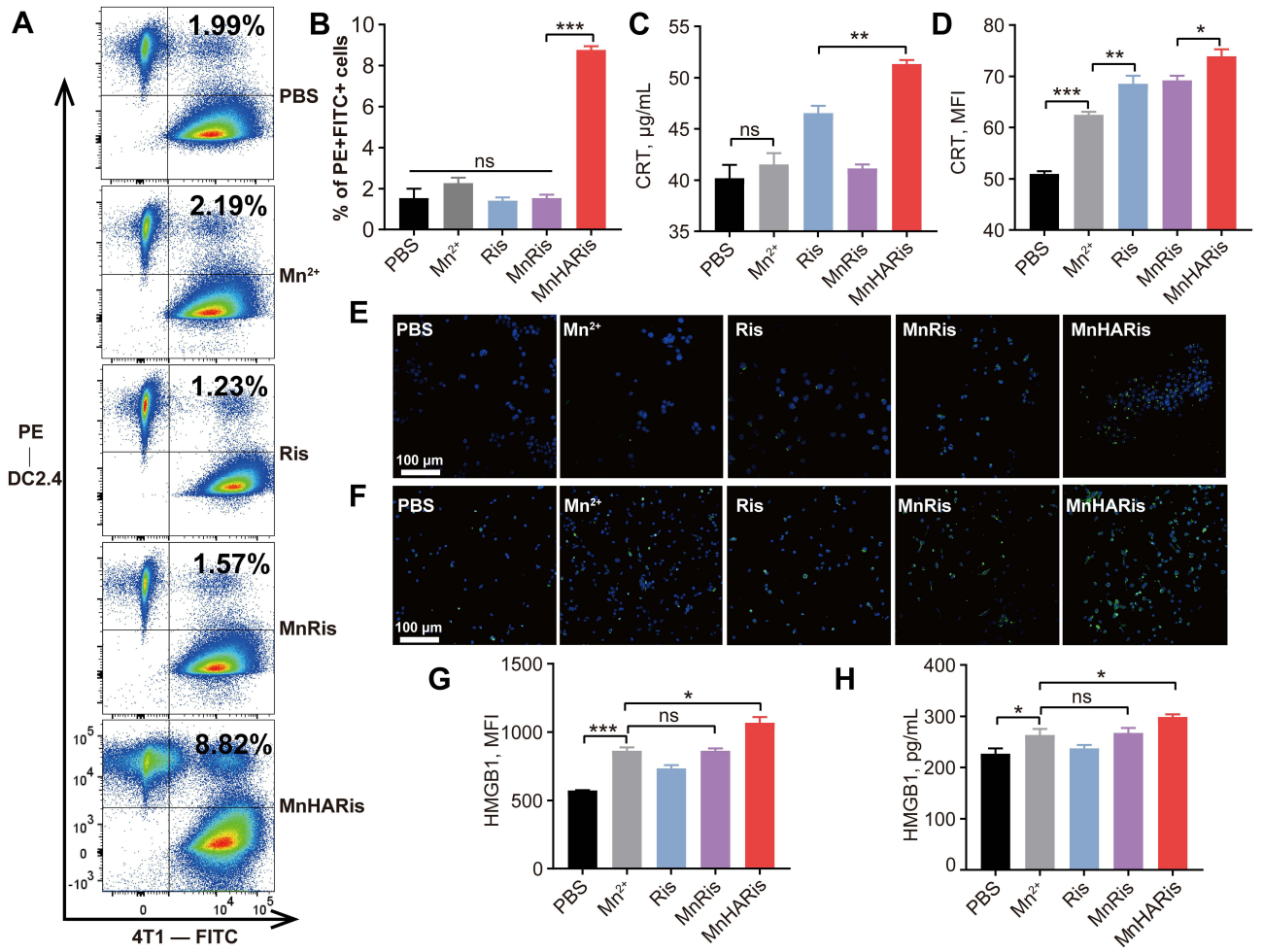

Figure 3 In Vitro Phagocytosis and ICD Marker Analysis. (**A**) Representative pictures of in vitro phagocytosis of the dying 4T1 tumor cells (FITC) by DC2.4 cells (PE) as analyzed by FCM and the quantized result (**B**). (**C**) CRT expression levels detected using an ELISA kit after treated with PBS, Mn^{2+}, Ris, MnRis, and MnHARis in 4T1 cells. (**D**) FCM analysis of cells expressing CRT on their membrane surface. (**E**) Representative CLSM images showing CRT localization on the cell membrane (scale bar=100 μm). (**F**) Representative CLSM images of HMGB1 and its quantified result plots verified using FCM (**G**). The HMGB1 concentrations in different group measured by ELISA and (**H**). Statistical significance was defined as *p < 0.05, **p < 0.01, ***p < 0.001.

MnHARis' Possible Antitumor Mechanisms

RNA sequencing results (RNA-Seq) conducted on 4T1 cells treated with PBS or MnHARis for 24 hours revealed significant modulation of pathways involved in genetic material processing (DNA replication, homologous recombination, mismatch repair, cell cycle, base excision repair, focal adhesion), inflammation (IL-17 and TNF signaling pathways), and apoptosis (p53 and MAPK signaling pathways, Figure 4A). MnHARis treatment also notably upregulated pathways such as Toll-like receptor signaling, C-type lectin receptor signaling, and NOD-like receptor signaling (Figure 4B), supporting its role in ICD and the generation of DAMPs which activate pattern recognition receptors (PRRs). RNA sequencing results prompted us to further validate the effects of MnHARis on cell cycle and MAPK pathway. The cell cycle of each treatment group was blocked in S phase to varying degrees (Figure 4C). To further investigate the role of autophagy in MnHARis-induced apoptosis of 4T1 cancer cells, we used 3-MA, a classical inhibitor of autophagy, to block autophagy and then calculated the cell viability of the exposed 4T1 cells with or without pre-treatment with 3-MA. As shown in Figure 4D, 3-MA pre-treatment markedly enhanced the cell viability of MnHARis-incubated 4T1 cells. Inhibiting mitochondrial autophagy by mdivi-1 could also significantly attenuate MnHARis-induced mitochondrial dysfunction and alleviate the cytotoxicity induced by MnHARis on 4T1 cells (Figure 4E). Wor can effectively inhibited Polo-like kinase 1 (PlK1) and Plk3 and SB202190 is an autophagy inducer and specific p38 inhibitor.[20] Apparently MnHARis-induced apoptosis and autophagy were abrogated by Wor and SB202190 (Figure 4F

https://doi.org/10.2147/IJN.S502394

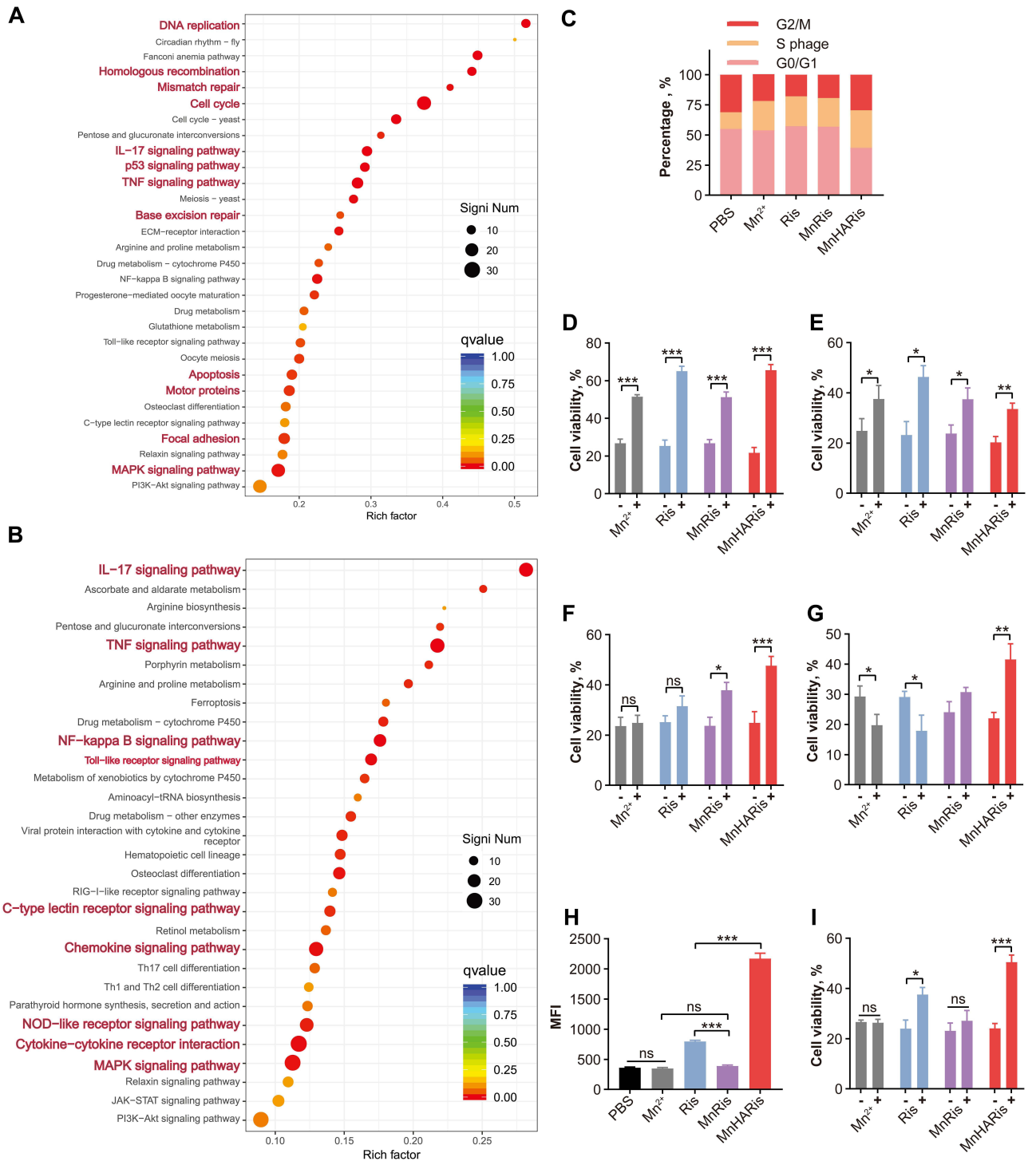

Figure 4 Impact of MnHARis on p38 MAPK Signaling, Cell Cycle Progression and Ca^{2+} overload. (**A**) Bubbles of KEGG pathways for differential gene enrichment. The circle presented gene number. The color of circles indicates the Q value. (**B**) KEGG pathway bubbles enriched by up-regulated differential genes. (**C**) Cell cycle phase distribution in 4T1 cells following 24-hour treatments of PBS, Mn^{2+}, Ris, MnRis and MnHARis in 4T1 cells. Effects of pretreatment with 5 mm 3-MA (**D**), 10 μM Mdivi (**E**), 10 μM Wor (**F**) or 10 μM SB202190 (**G**) on the cytotoxicity in 4T1 cells after different treatments measured by CCK8 assay. (**H**) Intracellular Ca^{2+} levels detected by Fluo-4 AM. (**I**) Effects of 5 μM BAPTA-AM pretreatment on the cell viability of 4T1 cells upon $MnCl_2$, Ris, MnRis or MnHARis treatment for 48 h. Statistical significance was defined as *p < 0.05, **p < 0.01, ***p < 0.001.

and G). Significantly, Wor did not affect the cytotoxicity induced by $MnCl_2$ and Ris, while SB202190 enhanced the cytotoxicity induced by Mn^{2+} and Ris on 4T1 cells. This may indicate that soluble forms of Mn^{2+} and Ris cannot induce apoptosis in tumor cells through the p38 MAPK pathway, whereas MnHARis formed by both with HA mineralization can. Additionally, HA and Ris are known to induce apoptosis in cancer cells,[21,22] and MnHARis, formed through Mn^{2+} and Ris mineralization with HA, raised the possibility that calcium (Ca) overload could be a mechanism of action (Figure 4H). This was further supported by the observation that exposure to Ris and MnHARis led to a rise in intracellular Ca^{2+} levels, and that chelation of intracellular Ca^{2+} with BAPTA-AM inhibited MnHARis-induced Ca^{2+} overload and apoptosis (Figure 4I).

MnHARis Synergizes with Immune Checkpoint Inhibitors (ICIs) Against Tumors

The combined application of ICD inducers and Immune Checkpoint Blockade (ICB) may synergistically enhance antitumor activity.[26] To evaluate the anti-tumor effect of MnHARis and its synergistic potential with anti-PD-L1 (αPD-L1) antibody, we established 4T1 tumor model and human hepatocellular PDX. As shown in Figure 5A and B, compared with the control group (1774.1 ± 218.3 mm^3), intratumoral injection of MnHAR (1144.2 ± 67.2 mm^3) significantly reduced the tumor volume of 4T1 and significantly prolonged the survival period. The combination of MnHARis and αPD-L1 antibody (666.8 ± 95.3 mm3) showed better antitumor effects than using MnHARis alone. And the intratumoral administration of MnHARis or MnHARis combined with αPD-L1 antibody had no significant effect on the body weight of mice (Figure 5C). Subsequently, we collected endpoint tumors from mice (on day 15) and analyzed tumor-infiltrating T cells through IHC (Figure 5D and E). Both $CD4^+$ T (Figure 5D) and $CD8^+$ T cells (Figure 5E) in the tumor were significantly increased by the MnHARis treatment, suggesting the alleviation of immunosuppression and the enhanced tumor-specific cytotoxic T lymphocytes response. To further validate the role of the immune system in MnHARis' antitumor effects, a human hepatocellular PDX was established using severely immunodeficient NOD SCID mice. The absence of a significant difference in tumor volume between the MnHARis-treated and PBS control groups highlighted the necessity of an active immune system for MnHARis' antitumor action (Figure 5F and G). No significant body weight loss was observed in the two groups (Figure 4H). Collectively, these findings underscore the potential of MnHARis treatment to enhance the efficacy of ICB therapy by modulating the tumor immune microenvironment.

Discussion

In this study, the enhanced cytotoxicity of MnHARis compared to MnRis can be partially attributed to the Ca^{2+} overload effect induced by the introduction of Ca^{2+} in HA, the synergistic amplification of ICD effects induced by Mn^{2+} and Ris, the sustained release of Mn^{2+} and Ris by HA, and the activation of the p38-MAPK pathway. Significant advancements have been made in Mn-based immunotherapy for cancer treatment, yet the field continues to present both opportunities and challenges.[18] For instance, the efficacy of Mn-based immunotherapy alone is often limited by the heterogeneity and diversity of tumors as well as the complex immunosuppressive TME. To enhance the antitumor immune response, Mn-based materials are frequently combined with other immuno-activators to bolster the immunotherapeutic effect. BPs (eg, Ris) are potent enhancers for Mn-based materials in inducing ICD. They contribute to the accumulation of phosphorylated antigens, increase cytotoxicity, enhance γδ T cell activity in the TME, and elevate cytokine secretion.[27] BPs inhibit farnesyl diphosphate synthase and exhibit cytotoxic effects against cancer cells both as a monotherapy and in sensitizing tumor cells to destruction by γδ T cells.[28] Mn^{2+} initially triggers ICD by activating the intracellular type I interferon response through the cGAS-STING pathway. With the aid of γδ T cells activated by Ris, it further enhances the adaptive immune response, facilitating the successful completion of the ICD process and amplifying the ICD effect.

ICD is a type of immune regulatory cell death that induces adaptive T cells against dead cell-associated antigens.[29] MnHARis help three determinants of ICD process smoothly. First, the dying cells shall express antigens must not fully covered by thymic tolerance. MnHARis not only induces autophagic apoptosis of tumor cells through cytotoxicity, increasing the emergence of recognizable dead cell-associated antigens, but also stimulates ICD by activating the cGAS-STING pathway, producing highly immunogenic tumor cell debris and type I interferon. Second, cell death must be accompanied by the emission of adjuvant-like signals that promote the recruitment and activation of APCs. Our previous study showed that MnHARis had good adjuvant activity and APC activation effect,[20] and the better phagocytosis of dead 4T1 cells by DC2.4

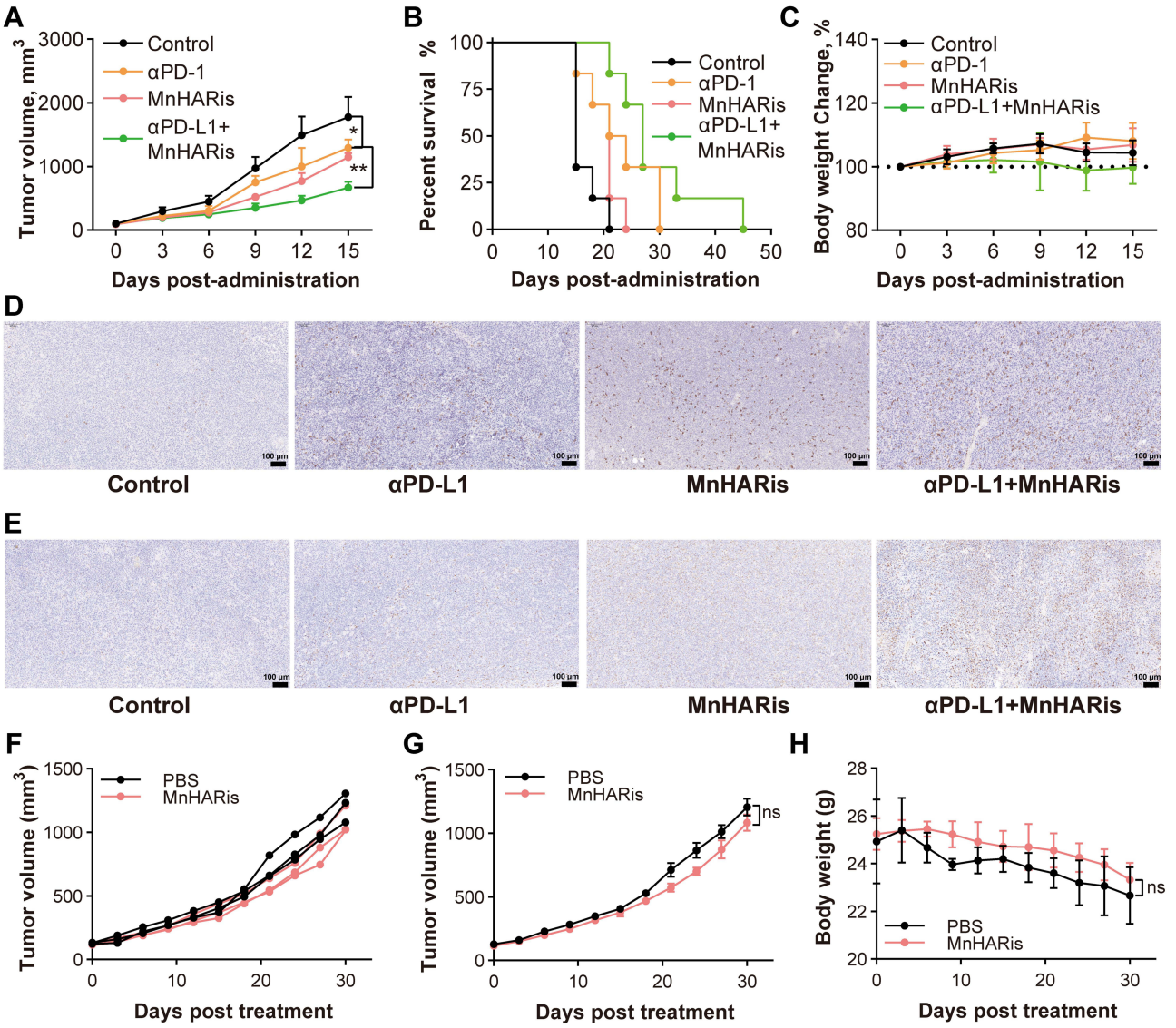

Figure 5 In Vivo Tumor Growth Inhibition and Immune Modulation by MnHARis. (**A**) Tumor volume changes and the corresponding survival (**B**) over experimental period. (**C**) Body weight change curve. BALB/c mice were intratumor inject with PBS (50 μL/dose), 50 μL MnHARis (50 μL/dose), αPD-L1 (100 μg/dose) or MnHARis + αPD-L1 every 3 days (total 4 doses, n=6). IHC images of tumor sections stained with antibodies against mouse $CD4^+$ (**D**) and $CD8^+$ (**E**) (scale bar: 100 μm). (**F**) Individual tumour growth curves, average tumor volume (**G**) and changes in body weight (**H**) for NOD SCID mice treated with PBS (50 μL/dose) or MnHARis (50 μL/dose) every 3 days (total 4 doses, n=3). Statistical significance was defined as *p < 0.05, **p < 0.01, ***p < 0.001.

cells after treatment with MnHARis confirmed that MnHARis supports the second prerequisite of ICD. Third, tumor microenvironmental conditions must be permissive for APC recruitment, activation, and migration to lymph nodes for $CD8^+$ T-cell cross-priming. MnHARis enhances the exposure of endoplasmic reticulum chaperones such as CRT on the surface of malignant cells and the release of HMGB1, initiating a type I interferon response. This sequence of events recruits and activates APCs to uptake cellular debris, promoting the innate immune response and establishing an adaptive immune response.

Progress can also be made in the areas of material preparation, mechanism exploration, application promotion, and evaluation of biological performance to advance the development and clinical translation of Mn-based tumor immunotherapy. The biomimetic mineralization strategy offers a simple, practical, and reproducible synthesis method, making it a preferred approach for preparing Mn-based materials. BPs, a class of bone treatment drugs, bind to metal ions with the highest affinity for Ca^{2+}.[30] Utilizing HA to mineralize Mn^{2+} and BPs to form MnHARis employs a simple and scalable "T" mixing technique. This method not only ensures complete precipitation of the components to form stable slow-release particles but also enhances

the antitumor effects and biocompatibility of the active ingredients. The sustained release of active antitumor components (Mn^{2+} and Ris) helps to enhance the killing effect of MnHARis on tumor cells. While CRT, HMGB1, and ATP are considered central to the immunogenic potential of ICD inducers, with extracellular ATP and HMGB1 serving as "find-me" signals and ecto-CRT as an "eat-me" signal, not all ICD inducers trigger the same stress responses or molecular signaling, leading to variability in results across different studies.[31–34] MnHARis induced ICD accompanied by enhanced CRT and HMGB1 signaling but attenuated ATP signaling. ROS-induced autophagy, such as that seen in hypericin-based photodynamic therapy, can negatively regulate CRT exposure by mitigating oxidative stress, without affecting ATP secretion.[35] Consequently, diverse inducers might exert different impact on ICD, partially due to discrepancy in signaling pathways as well as cell lines.

Although the widely accepted immunological mechanism involves the activation of the cGAS-STING pathway by Mn^{2+}, Mn-based nanomaterials may activate many other hidden mechanisms.[36] MnHARis may exert a synergistic antitumor effect by enhancing the activation of the p38-MAPK pathway by Mn^{2+} and Ris. The apoptosis process induced by Mn^{2+} is associated with the p38-MAPK pathway;[37] however, the concentration of Mn^{2+} used in this study exhibits a weak activation effect on the p38-MAPK pathway. BPs can exert antitumor effects synergistically through the mevalonate pathway and the p38-MAPK pathway.[38,39] The HA mineralization of Mn^{2+} and Ris enhances the activation of the p38-MAPK pathway by MnHARis, enabling lower concentrations of Mn^{2+} and Ris to effectively exert antitumor effects. The exact pathway of MnHARis activation of the p38-MAPK pathway has not been determined. The production of ROS can trigger p38-MAPK activation.[40] Since the production of ROS is often associated with metal exposure,[41] excessive ROS production is a possible reason for MnHARis-induced apoptosis. Within the lethal concentration range, both Mn^{2+} and Ris can induce ROS production, and excessive ROS can cause mitochondrial-mediated apoptosis.[42] However, in this study, low concentrations of Mn^{2+} or Ris alone were not able to induce excessive ROS production. The mineralization of Mn^{2+} and Ris using HA can synergistically exert their induction of ROS, further leading to mitochondrial membrane potential disruption, potent activation of the p38-MAPK pathway, and enhanced antitumor effects. In the future, MnHARis can be combined with anti-tumor measures such as cold exposure therapy,[43] photodynamic[44] and nano-catalytic treatments[45] to further increase ROS production within tumors, thereby significantly inhibiting tumor growth and recurrence.

The combined application of Mn^{2+} and Ris induced synergistic antiproliferative and pro-apoptotic effects in nine cell lines. By co-applying HA-mineralized Mn^{2+} and Ris, we found a 17-fold reduction in the IC_{50} dose compared to monotherapy. We also validated the significant synergistic effects of Mn^{2+} and Ris in a cervical cancer PDO model. Consistent with in vitro data, the combination of MnHARis and αPD-L1 antibody exhibited synergistic antitumor effects in the 4T1 tumor-bearing mouse model. Although we did not observe evidence of tumor regression, we found that the combination of MnHAR and αPD-L1 antibody therapy had a more significant inhibitory effect on tumor growth compared to monotherapy. Additionally, there were more notable histopathological changes, such as higher apoptotic activity and a greater number of tumor-infiltrating T cells. In the combination therapy, no increase in weight loss or other signs of acute or delayed toxicity were observed in vivo. Mechanistically, compared with monotherapy, the combination of MnHAR and αPD-L1 antibody can synergistically delay tumor growth, potentially due to ICD leading to the transformation of an immunosuppressive "cold" TME into an immunologically active "hot" TME with increased $CD4^+$ T cells and $CD8^+$ T cells. TNBC is characterized by high malignancy, early metastasis, limited treatment options, and poor prognosis.[46] Immunotherapy, as an emerging and most promising cancer treatment strategy, has limited efficacy in triple-negative breast cancer due to the immunosuppressive nature of TME. Recent studies have shown that higher TILs content in tumor tissues is associated with better survival, and the abundance of TILs may serve as a prognostic marker, potentially aiding in providing optimal treatment plans for individual patients.[47] Therefore, MnHARis is a potential candidate for sensitizing TNBC to anti-PD-L1 therapy.

Finally, systematically evaluating the biological performance and biosafety of Mn-based platforms is crucial, including aspects such as cytotoxicity, blood compatibility and pharmacokinetics. This is also a limitation of this study. Based on the evaluation of its biosafety, we highly anticipate that Mn-based immunotherapy will pave a promising path for tumor immunotherapy.

Conclusions

Although anti-PD-L1 immunotherapy offers a promising approach for TNBC treatment, its efficacy is often limited by low response rates and therapeutic resistance resulting from the immunosuppressive TME. By utilizing HA mineralized with Mn^{2+} and Ris, MnHARis particles with high biocompatibility and sustained release properties were developed. Compared to Mn^{2+} or Ris alone, MnHARis significantly increased toxicity towards tumor cell proliferation, reducing the IC_{50} by 17-fold. Mechanistic studies indicated that MnHARis promoted apoptosis via mitochondrial autophagy, evidenced by nuclear fragmentation, elevated ROS levels, decreased ATP levels, mitochondrial membrane depolarization, and upregulation of autophagy markers LC3B and Beclin. Additionally, MnHARis facilitated the activation of dendritic cells and PRRs by increasing CRT exposure and HMGB1 secretion, thereby inducing ICD. This process altered the TME and enhanced the immune response of tumor-infiltrating $CD8^+$ T cells. In vivo experiments demonstrated that the combination of MnHARis with anti-PD-L1 antibodies exhibited significant synergistic antitumor effects in 4T1 tumor-bearing mouse models. MnHARis effectively synergized Mn^{2+} and Ris to promote autophagic apoptosis, induce ICD, and enhance $CD8^+$ T cell immunity within tumors. Therefore, MnHARis holds potential for sensitizing TNBC to anti-PD-L1 therapy by increasing TILs.

Ethics Statement

Experiments involving mice were reviewed and approved by the Animal Care and Use Committee of Xiamen University (XMULAC20220301). The manipulation and vaccination of animals strictly adhered to and complied with the guidelines provided by XMULAC. All procedures adhered strictly to animal ethics guidelines and approved protocols to ensure minimum suffering during vaccination, blood collection, and euthanasia.

Acknowledgments

This study was supported by National Key Research and Development Program through grants No. 2023YFC2307602, National Natural Science Foundation of China through grants No. 82271873, NO. 82171821 and No. 82473313, Xiamen Natural Science Foundation through grants No. 3502Z20227165, Xiang'an Innovation Laboratory through grants No. 2023XAKJ0101019 and No. 2023XAKJ0101038, and the Fundamental Research Funds for the Central Universities through grants No. 20720220004 and 20720220006.

Disclosure

The authors hereby declare that there are no known competing financial interests or personal relationships that could have potentially influenced the work reported in this paper.

References

1. Costa A, Kieffer Y, Scholer-Dahirel A, et al. Fibroblast Heterogeneity and immunosuppressive environment in human breast cancer. *Cancer Cell*. 2018;33(3):463–479e410. doi:10.1016/j.ccell.2018.01.011
2. Grinda T, Antoine A, Jacot W, et al. Evolution of overall survival and receipt of new therapies by subtype among 20 446 metastatic breast cancer patients in the 2008–2017 ESME cohort. *ESMO Open*. 2021;6(3):100114. doi:10.1016/j.esmoop.2021.100114
3. Zhang Y, Chen H, Mo H, et al. Single-cell analyses reveal key immune cell subsets associated with response to PD-L1 blockade in triple-negative breast cancer. *Cancer Cell*. 2021;39(12):1578–1593e1578. doi:10.1016/j.ccell.2021.09.010
4. Mittendorf EA, Zhang H, Barrios CH, et al. Neoadjuvant atezolizumab in combination with sequential nab-paclitaxel and anthracycline-based chemotherapy versus placebo and chemotherapy in patients with early-stage triple-negative breast cancer (IMpassion031): a randomised, double-blind, Phase 3 trial. *Lancet*. 2020;396(10257):1090–1100. doi:10.1016/S0140-6736(20)31953-X
5. Jiang Z, Ouyang Q, Sun T, et al. Toripalimab plus nab-paclitaxel in metastatic or recurrent triple-negative breast cancer: a randomized phase 3 trial. *Nat Med*. 2024;30(1):249–256. doi:10.1038/s41591-023-02677-x
6. Schmid P, Adams S, Rugo HS, et al. Atezolizumab and nab-paclitaxel in advanced triple-negative breast cancer. *N Engl J Med*. 2018;379(22):2108–2121. doi:10.1056/NEJMoa1809615
7. Sanmamed MF, Berraondo P, Rodriguez-Ruiz ME, Melero I. Charting roadmaps towards novel and safe synergistic immunotherapy combinations. *Nat Cancer*. 2022;3(6):665–680. doi:10.1038/s43018-022-00401-1
8. Fucikova J, Kepp O, Kasikova L, et al. Detection of immunogenic cell death and its relevance for cancer therapy. *Cell Death Dis*. 2020;11(11):1013. doi:10.1038/s41419-020-03221-2
9. Yan M, Chen Q, Liu T, et al. Site-selective superassembly of biomimetic nanorobots enabling deep penetration into tumor with stiff stroma. *Nat Commun*. 2023;14(1):4628. doi:10.1038/s41467-023-40300-2

10. Himelstein AL, Foster JC, Khatcheressian JL, et al. Effect of longer-interval vs standard dosing of zoledronic acid on skeletal events in patients with bone metastases: a randomized clinical trial. *JAMA*. 2017;317(1):48–58. doi:10.1001/jama.2016.19425
11. Coleman RE, Marshall H, Cameron D, et al. Breast-cancer adjuvant therapy with zoledronic acid. *N Engl J Med*. 2011;365(15):1396–1405. doi:10.1056/NEJMoa1105195
12. Van Acker HH, Anguille S, Willemen Y, Smits EL, Van Tendeloo VF. Bisphosphonates for cancer treatment: mechanisms of action and lessons from clinical trials. *Pharmacol Ther*. 2016;158:24–40. doi:10.1016/j.pharmthera.2015.11.008
13. Wada A, Fukui K, Sawai Y, et al. Pamidronate induced anti-proliferative, apoptotic, and anti-migratory effects in hepatocellular carcinoma. *J Hepatol*. 2006;44(1):142–150. doi:10.1016/j.jhep.2005.09.022
14. Senaratne SG, Mansi JL, Colston KW. The bisphosphonate zoledronic acid impairs Ras membrane [correction of impairs membrane] localisation and induces cytochrome c release in breast cancer cells. *Br J Cancer*. 2002;86(9):1479–1486. doi:10.1038/sj.bjc.6600297
15. Nakajima H, Magae J, Tsuruga M, et al. Induction of mitochondria-dependent apoptosis through the inhibition of mevalonate pathway in human breast cancer cells by YM529, a new third generation bisphosphonate. *Cancer Lett*. 2007;253(1):89–96. doi:10.1016/j.canlet.2007.01.008
16. Sewing L, Steinberg F, Schmidt H, Goke R. The bisphosphonate zoledronic acid inhibits the growth of HCT-116 colon carcinoma cells and induces tumor cell apoptosis. *Apoptosis*. 2008;13(6):782–789. doi:10.1007/s10495-008-0211-z
17. Teixeira S, Branco L, Fernandes MH, Costa-Rodrigues J. Bisphosphonates and Cancer: a Relationship Beyond the Antiresorptive Effects. *Mini Rev Med Chem*. 2019;19(12):988–998. doi:10.2174/1389557519666190424163044
18. Zhang K, Qi C, Cai K. Manganese-Based Tumor Immunotherapy. *Adv Mater*. 2023;35(19):e2205409. doi:10.1002/adma.202205409
19. Ding B, Zheng P, Ma P, Lin J. Manganese oxide nanomaterials: synthesis, properties, and theranostic applications. *Adv Mater*. 2020;32(10):e1905823. doi:10.1002/adma.201905823
20. Zhang X, Wei M, Zhang Z, et al. Risedronate-functionalized manganese-hydroxyapatite amorphous particles: a potent adjuvant for subunit vaccines and cancer immunotherapy. *J Control Release*. 2024;367:13–26. doi:10.1016/j.jconrel.2024.01.033
21. Xu Y, Tang H, Wu P, et al. Manganese-doped hydroxyapatite as an effective adsorbent for the removal of Pb(II) and Cd(II). *Chemosphere*. 2023;321:138123. doi:10.1016/j.chemosphere.2023.138123
22. Lin KL, Chang J, Liu XG, Chen L, Zhou YL. Synthesis of element-substituted hydroxyapatite with controllable morphology and chemical composition using calcium silicate as precursor. *Crystengcomm*. 2011;13(15):4850–4855. doi:10.1039/c0ce00835d
23. Lin Y, Liu N, Yang C, et al. Oncolytic activity of a coxsackievirus B3 strain in patient-derived cervical squamous cell carcinoma organoids and synergistic effect with paclitaxel. *Virol J*. 2024;21(1):245. doi:10.1186/s12985-024-02502-y
24. Wang Q, Ju X, Wang J, Fan Y, Ren M, Zhang H. Immunogenic cell death in anticancer chemotherapy and its impact on clinical studies. *Cancer Lett*. 2018;438:17–23. doi:10.1016/j.canlet.2018.08.028
25. Bianchi ME, Crippa MP, Manfredi AA, Mezzapelle R, Rovere Querini P, Venereau E. High-mobility group box 1 protein orchestrates responses to tissue damage via inflammation, innate and adaptive immunity, and tissue repair. *Immunol Rev*. 2017;280(1):74–82. doi:10.1111/imr.12601
26. Yu S, Xiao H, Ma L, Zhang J, Zhang J. Reinforcing the immunogenic cell death to enhance cancer immunotherapy efficacy. *Biochim Biophys Acta Rev Cancer*. 2023;1878(5):188946. doi:10.1016/j.bbcan.2023.188946
27. Frieling JS, Tordesillas L, Bustos XE, et al. gammadelta-Enriched CAR-T cell therapy for bone metastatic castrate-resistant prostate cancer. *Sci Adv*. 2023;9(18):eadf0108. doi:10.1126/sciadv.adf0108
28. Hodgins NO, Wang JT, Al-Jamal KT. Nano-technology based carriers for nitrogen-containing bisphosphonates delivery as sensitisers of gamma-delta T cells for anticancer immunotherapy. *Adv Drug Deliv Rev*. 2017;114:143–160. doi:10.1016/j.addr.2017.07.003
29. Petroni G, Buque A, Zitvogel L, Kroemer G, Galluzzi L. Immunomodulation by targeted anticancer agents. *Cancer Cell*. 2021;39(3):310–345. doi:10.1016/j.ccell.2020.11.009
30. Moreira MP, de Almeida Soares GD, Dentzer J, et al. Synthesis of magnesium- and manganese-doped hydroxyapatite structures assisted by the simultaneous incorporation of strontium. *Mater Sci Eng C Mater Biol Appl*. 2016;61:736–743. doi:10.1016/j.msec.2016.01.004
31. Liu Y, Wang Y, Yang Y, et al. Emerging phagocytosis checkpoints in cancer immunotherapy. *Signal Transduct Target Ther*. 2023;8(1):104. doi:10.1038/s41392-023-01365-z
32. Michaud M, Martins I, Sukkurwala AQ, et al. Autophagy-dependent anticancer immune responses induced by chemotherapeutic agents in mice. *Science*. 2011;334(6062):1573–1577. doi:10.1126/science.1208347
33. Yamazaki T, Kirchmair A, Sato A, et al. Mitochondrial DNA drives abscopal responses to radiation that are inhibited by autophagy. *Nat Immunol*. 2020;21(10):1160–1171. doi:10.1038/s41590-020-0751-0
34. Galluzzi L, Vitale I, Warren S, et al. Consensus guidelines for the definition, detection and interpretation of immunogenic cell death. *J Immunother Cancer*. 2020;8(1):e000337. doi:10.1136/jitc-2019-000337
35. Garg AD, Dudek AM, Ferreira GB, et al. ROS-induced autophagy in cancer cells assists in evasion from determinants of immunogenic cell death. *Autophagy*. 2013;9(9):1292–1307. doi:10.4161/auto.25399
36. Yi L, Jiang X, Zhou Z, et al. A hybrid nanoadjuvant simultaneously depresses PD-L1/TGF-beta1 and activates cGAS-STING pathway to overcome radio-immunotherapy resistance. *Adv Mater*. 2024;36(15):e2304328. doi:10.1002/adma.202304328
37. El Mchichi B, Hadji A, Vazquez A, Leca G. p38 MAPK and MSK1 mediate caspase-8 activation in manganese-induced mitochondria-dependent cell death. *Cell Death Differ*. 2007;14(10):1826–1836. doi:10.1038/sj.cdd.4402187
38. Bruzzese F, Pucci B, Milone MR, et al. Panobinostat synergizes with zoledronic acid in prostate cancer and multiple myeloma models by increasing ROS and modulating mevalonate and p38-MAPK pathways. *Cell Death Dis*. 2013;4(10):e878. doi:10.1038/cddis.2013.406
39. Merrell MA, Wakchoure S, Lehenkari PP, Harris KW, Selander KS. Inhibition of the mevalonate pathway and activation of p38 MAP kinase are independently regulated by nitrogen-containing bisphosphonates in breast cancer cells. *Eur J Pharmacol*. 2007;570(1–3):27–37. doi:10.1016/j.ejphar.2007.05.075
40. Ito S, Kuromiya K, Sekai M, et al. Accumulation of annexin A2 and S100A10 prevents apoptosis of apically delaminated, transformed epithelial cells. *Proc Natl Acad Sci U S A*. 2023;120(43):e2307118120. doi:10.1073/pnas.2307118120
41. Lopez-Blazquez C, Lacalle-Gonzalez C, Sanz-Criado L, Ochieng' Otieno M, Garcia-Foncillas J, Martinez-Useros J. Iron-dependent cell death: a new treatment approach against pancreatic ductal adenocarcinoma. *Int J Mol Sci*. 2023;24(19):14979. doi:10.3390/ijms241914979
42. Liu D, Du J, Sun J, Li M. Parathyroid hormone-related protein inhibits nitrogen-containing bisphosphonate-induced apoptosis of human periodontal ligament fibroblasts by activating MKP1 phosphatase. *Bioengineered*. 2021;12(1):1997–2006. doi:10.1080/21655979.2021.1928930

43. Chen Z, Liu Z, Zhou Y, et al. Bionic aggregation-induced emission photosensitizer for enhanced cancer immunotherapy. *Mater Today Bio*. 2024;28:101217. doi:10.1016/j.mtbio.2024.101217
44. Ning S, Zhang T, Lyu M, et al. A type I AIE photosensitiser-loaded biomimetic nanosystem allowing precise depletion of cancer stem cells and prevention of cancer recurrence after radiotherapy. *Biomaterials*. 2023;295:122034. doi:10.1016/j.biomaterials.2023.122034
45. Zhang N, Ping W, Xiang J, et al. Biomimetic single-atom nanozyme for dual starvation-enhanced breast cancer immunotherapy. *Adv Healthc Mater*. 2024;14(8):e2401362. doi:10.1002/adhm.202401362
46. Bianchini G, De Angelis C, Licata L, Gianni L. Treatment landscape of triple-negative breast cancer - expanded options, evolving needs. *Nat Rev Clin Oncol*. 2022;19(2):91–113. doi:10.1038/s41571-021-00565-2
47. Leon-Ferre RA, Jonas SF, Salgado R, et al. Tumor-infiltrating lymphocytes in triple-negative breast cancer. *JAMA*. 2024;331(13):1135–1144. doi:10.1001/jama.2024.3056